

UC Santa Cruz

UC Santa Cruz Previously Published Works

Title

An optimization algorithm for dose reduction with fluence-modulated proton CT.

Permalink

<https://escholarship.org/uc/item/55n9w7g0>

Journal

Medical physics, 47(4)

ISSN

0094-2405

Authors

Dickmann, J
Rit, S
Pankuch, M
[et al.](#)

Publication Date

2020-04-01

DOI

10.1002/mp.14084

Peer reviewed

An optimization algorithm for dose reduction with fluence–modulated proton CT

J. Dickmann¹, S. Rit², M. Pankuch³, R. P. Johnson⁴,
R. W. Schulte⁵, K. Parodi¹, G. Dedes^{1,a}, G. Landry^{6,7,1,a,b}

¹ Department of Medical Physics, Faculty of Physics, Ludwig-Maximilians-Universität München,
Am Coulombwall 1, 85748 Garching b. München, Germany

² Univ Lyon, INSA-Lyon, Université Claude Bernard Lyon 1, UJM-Saint Étienne, CNRS, Inserm,
CREATIS UMR 5220, U1206, F-69373, Lyon, France

³ Northwestern Medicine Chicago Proton Center, Warrenville, IL 60555, United States of
America

⁴ Department of Physics, University of California Santa Cruz, Santa Cruz, CA 95064, United
States of America

⁵ Division of Biomedical Engineering Sciences, Loma Linda University, Loma Linda, CA 92354,
United States of America

⁶ Department of Radiation Oncology, University Hospital, LMU Munich, 81377 Munich,
Germany

⁷ German Cancer Consortium (DKTK), 81377 Munich, Germany

^a Senior authorship is shared equally.

^b Author to whom correspondence should be addressed. email:

guillaume.landry@med.uni-muenchen.de

Abstract

Purpose: Fluence–modulated proton computed tomography (FMpCT) using pencil beam scanning aims at achieving task–specific image noise distributions by modulating the imaging proton fluence spot–by–spot based on an object–specific noise model. In this work we present a method for fluence field optimization and investigate its performance in dose reduction for various phantoms and image variance targets.

Methods: The proposed method uses Monte Carlo simulations of a proton CT (pCT) prototype scanner to estimate expected variance levels at uniform fluence. Using an iterative approach, we calculate a stack of target variance projections that are required to achieve the prescribed image variance, assuming a reconstruction using filtered back-projection. By fitting a pencil beam model to the ratio of uniform fluence variance and target variance, relative weights for each pencil beam can be calculated. The quality of the resulting fluence modulations is evaluated by scoring imaging doses and comparing them to those at uniform fluence, as well as evaluating conformity of the achieved variance with the prescription. For three different phantoms, we prescribed constant image variance as well as two regions–of–interest (ROI) imaging tasks with inhomogeneous image variance. The shape of the ROIs followed typical beam profiles for proton therapy.

Results: Prescription of constant image variance resulted in a dose reduction of 8.9% for a homogeneous water phantom compared to a uniform fluence scan at equal peak

variance level. For a more heterogeneous head phantom, dose reduction increased to 16.0% for the same task. Prescribing two different ROIs resulted in dose reductions between 25.7% and 40.5% outside of the ROI at equal peak variance levels inside the ROI. Imaging doses inside the ROI were increased by 9.2% to 19.2% compared to the uniform fluence scan, but can be neglected assuming that the ROI agrees with the therapeutic dose region. Agreement of resulting variance maps with the prescriptions was satisfactory.

Conclusions: We developed a method for fluence field optimization based on a noise model for a real scanner used in proton computed tomography. We demonstrated that it can achieve prescribed image variance targets. A uniform fluence field was shown not to be dose optimal and dose reductions achievable with the proposed method for fluence-modulated proton CT were considerable, opening an interesting perspective for image guidance and adaptive therapy.

Keywords: proton CT, fluence field optimization, proton therapy, dose reduction, fluence-modulated proton CT

I. Introduction

Cancer treatment using intensity-modulated proton and heavier ion therapy is effective, and comes at a low risk of side-effects for the patient compared to conventional treatment modalities using x-rays. The good tolerance is believed to be linked to the low dose to normal tissue when using protons for treatment.¹⁻⁴ At the same time, low-dose, frequent and accurate imaging, ideally at the treatment site, is required to ensure a safe delivery of the therapeutic doses.^{5,6} Proton therapy treatment planning requires a spatial map of the relative (to water) stopping power (RSP), which in current clinical practice is acquired through a conversion from x-ray CT images.⁷⁻⁹ X-ray CT images are typically not acquired in treatment position and not prior to every treatment fraction, in order to keep treatment time short and imaging dose low enough that they do not compromise the dose benefit of proton therapy.¹⁰ Direct imaging of RSP using proton computed tomography (pCT)¹¹⁻¹⁶ has been proposed to increase accuracy and to allow for a frequent, dose efficient acquisition in treatment position. Accuracies achievable with current prototypes are comparable to state-of-the-art clinical dual energy x-ray CT.^{7,17-19}

A further reduction of imaging dose can be achieved by modulating the imaging fluence field during the acquisition and thereby achieving a task-specific image quality. Fluence-modulated scans²⁰ can either aim for homogeneous variance across the whole volume, or for region-of-interest imaging, where only the relevant part of the image is acquired at low noise and imaging dose is reduced elsewhere. Algorithms²¹⁻²⁴ and experimental prototypes²⁵⁻²⁹ have been developed for fluence modulation in x-ray CT. Recently, fluence-modulated pCT (FMpCT) has also been proposed³⁰ and its initial experimental feasibility using pencil beam scanning was investigated.³¹ The best achievable dose efficiency through fluence modulation or other techniques is a key requirement for x-ray CT³² and most likely will be for pCT as it moves closer to the clinics. Moreover, region-of-interest imaging is of high interest for particle therapy treatment planning and dose verification, where only a fraction of the image volume (the treatment beam path) is of relevance.³⁰ A challenge for FMpCT is that simple Poisson noise modeling is not sufficient, as image variance for pCT depends on the object's heterogeneity, and several contributions, including multiple Coulomb scattering, have to be taken into account for fluence-modulation.^{33,34}

In this work, we present a method for fluence-field optimization in pCT using pencil

beam scanning. We employ a pCT scanner-specific Monte Carlo simulation,³⁵ which was shown to reproduce experimental variance levels for a typical fluence field.³⁴ The problem of finding relative modulation factors for each pencil beam such that the summed fluence pattern results in a prescribed image variance map is a computationally expensive optimization problem which generally requires alternating between the reconstructed image domain (where the variance prescription is defined) and the projection domain (the detector data at each projection angle from which the image is reconstructed, and where the fluence modulation is defined). Therefore we separated the problem into first solving for the projection domain variance yielding a given prescribed variance in the image domain and subsequently optimizing pencil beam weights leading to this projection domain variance. To realistically describe pencil beams in the optimization and in simulations, we established a pencil beam model based on experimental data. In a simulation study, we estimated dose savings for fluence-modulated pCT using three different phantoms, and compared our proposed solution with a straightforward intersection-based fluence modulation.³¹ We also verified that the resulting variance map approaches the target variance. Both a constant variance target as well as two regions-of-interest (ROI) following typical treatment beam paths were investigated.

II. Materials and methods

II.A. Simulation framework

The Monte Carlo simulation framework³⁵ used in this study is a detailed model of the phase II pCT prototype scanner.¹³ It is based on the GEANT4 toolkit³⁶ version 10.2.p01. Details about the modeling of physics processes can be found in literature, where the platform was validated for its fidelity in terms of RSP.^{19,35} A previous study³⁴ improved the platform for reproducing variance levels of experimental scans. With respect to that work, the beam model was modified, and is described below. Imaging doses, in the form of absorbed physical dose, were scored on a centered grid of $125 \times 125 \times 35$ voxels with a uniform voxel size of 2 mm and summed for all projection angles.

The simulation framework outputs data in the same format as the prototype scanner. It records position and direction information of individual protons before and after the object,

as well as the proton’s residual energy. Using a calibration,³⁷ the residual energy can be mapped to a water-equivalent path length (WEPL), which is the line integral over the RSP of the object along the curved path of the proton. Because measurements are available for every detected proton, these data are referred to as “list-mode.”

II.B. Image reconstruction

To reconstruct RSP images from the list-mode data, a most likely path³⁸ is estimated for every proton from the tracking information. The path information is taken into account by performing distance-driven binning and applying a special cone-beam filtered backprojection algorithm.³⁹ In total, 90 projections from rotation angles covering a full rotation were used. This relatively low number of projections was chosen to satisfy experimental timing constraints and to allow for a future experimental validation of this work. Reconstructions were performed on a grid of $250 \times 250 \times 70$ voxels with a uniform size of 1 mm. For performing data cuts,^{12,38,39} the grid was 125×125 pixels with a uniform size of 2 mm. Binning of data into distance-driven projections was performed on a grid of $250 \times 250 \times 70$ voxels with a uniform size of 1 mm. All grids were centered on the isocenter.

Assume a voxel centered in (u, v, d) in the three-dimensional distance-driven projection, where d is the binning depth and u and v are the coordinates normal to it. We can identify a set of protons such that the most likely path of every proton crosses the voxel volume around (u, v, d) . The number of protons in that set is then referred to as the “counts” $C(u, v, d)$. These counts only consider protons used for image reconstruction and therefore are reduced compared to the incident protons due to interactions with the object and cuts on the data. In contrast to that, counts in the absence of interactions and cuts are referred to as $F(u, v, d)$ throughout the paper. The point $u = v = d = 0$ is the location of the isocenter, where the rotation axis is located.

II.C. Phantoms

In the simulation study, three different phantoms with a physical counterpart were used. The water phantom is a cylindrical container made from polystyrene (outer diameter 150.5 mm, wall thickness 6.35 mm) and filled with distilled water. The CTP404 phantom (*Phantom*

144 *Laboratory*, New York, USA) is a commercial sensitometric phantom with a cylindrical shape
 145 (diameter 150 mm) and several tissue-equivalent inserts and two cylinders filled with air.
 146 Both phantoms were implemented in the simulation as analytical models. The pediatric
 147 head phantom (ATOM[®], Model 715 HN, *CIRS Inc.*, Norfolk, USA) models the anatomy
 148 of a 5-year-old child and was implemented as a voxelized phantom in the simulation.⁴⁰
 149 Previous publications^{34,35,40} can be consulted for details about the phantoms.

150 II.D. Gaussian pencil beam model

151 To allow for the flexible simulation of FMpCT data, an analytical pencil beam model was
 152 derived from experimental tracking data acquired at the pencil beam scanning beamline
 153 of the Northwestern Medicine Chicago Proton Center without phantom. Using the timing
 154 information of the scanner, a count rate was calculated in steps of 0.8 ms, allowing for the
 155 separation of individual pencil beams as the count rate dropped in between two spots. The
 156 separated data were processed individually by estimating most likely paths and performing
 157 distance-driven binning.³⁹

158 For each pencil beam b , this resulted in a three-dimensional experimental counts map
 159 $C_b(u, v, d)$. We fitted the Gaussian model

$$160 \quad G(u, v, d) = \frac{N_0}{2\pi\sigma'_u\sigma'_v} \cdot \exp\left(-\frac{(u - u'_0(d))^2}{2\sigma'^2_u} - \frac{(v - v'_0(d))^2}{2\sigma'^2_v}\right) \quad (1)$$

161 to each pencil beam's C_b , where N_0 is the total number of protons per pencil beam, and
 162 $(u'_0(d), v'_0(d))$ is the pencil beam center at depth d . The pencil beam center is assumed
 163 to diverge linearly with the binning depth, such that $u'_0(d) = u_0 \cdot (1 + \delta_u \cdot d)$ and $v'_0(d)$
 164 analogously, where (u_0, v_0) is the pencil beam center at $d = 0$ and δ_u and δ_v are the linear
 165 divergence factors. By construction, the isocenter-beam for $u_0 = v_0 = 0$ is parallel to the
 166 d -axis. The $\sigma'_u = \sigma_u \cdot \sqrt{1 + \delta_u^2 d^2}$ and σ'_v analogously are the beam widths projected to a
 167 plane normal to the d -axis while σ_u and σ_v are the actual beam widths. This resulted in
 168 a fit with seven open parameters $(N_0, u_0, v_0, \sigma_u, \sigma_v, \delta_u, \delta_v)$, which was performed for each
 169 individual pencil beam by minimization of the squared deviation. The parameters $\sigma_u, \sigma_v, \delta_u$
 170 and δ_v were not specific to one pencil beam, and estimates for them were therefore found as
 171 the mean value over all pencil beams. N_0, v_0 and u_0 were open parameters specific to a given
 172 pencil beam, but overwritten in subsequent simulations of different pencil beam patterns.

They are therefore not reported.

II.D.1. Simulation of pencil beams

All datasets were generated by shooting a regular grid of simulated proton pencil beams. At $d = 0$, neighboring pencil beams were interspaced by $\Delta_{\text{PB},u} = 12 \text{ mm}$ along u and $\Delta_{\text{PB},v} = 8 \text{ mm}$ along v . The pencil beam grid was offset in u by $\Delta_{\text{PB},u}/4 = 3 \text{ mm}$ so that the summed fluence from two opposing angles was homogeneous. This helped to reduce the total number of pencil beams and thereby reduce the complexity of the optimization. In the simulation platform, protons were emitted from a point $(u_0 \cdot (1 + \delta_u \cdot d_0), v_0 \cdot (1 + \delta_v \cdot d_0), d_0) + (r_u, r_v, 0)$, where $d_0 = -400 \text{ mm}$ and r_u and r_v are normally distributed random numbers with a standard deviation of σ_u and σ_v respectively. The point d_0 is just before the front tracker and was chosen in agreement to previous investigations.³⁴ Protons were assumed to have an initial direction vector of $(u_0\delta_u, v_0\delta_v, 1)$. The beam centers (u_0, v_0) were chosen according the pencil beam grid defined above. For non-modulated scans, N_0 was set to a default value $N_0 = N$ for all pencil beams. For modulated scans it was $N_0 = m_b^\alpha N$ for a pencil beam modulated with a factor m_b^α . The proton's initial energy was set to $(200.00 \pm 0.66) \text{ MeV}$, which is the standard mean energy used experimentally. The energy spread was determined in a previous study³⁴ and agrees with experimental data acquired at the beamline at Northwestern Medicine Chicago Proton Center, albeit with a wider spot size setting.

II.D.2. Pencil beam reference counts

To optimize pencil beam weights, a reference of the proton counts for every pencil beam is needed. This reference serves as a basis function for the fluence modulation and should not take into account interactions with the object. It can be generated for every pencil beam b using the Gaussian model

$$F_b(u, v, d) = G(u, v, d) \Big|_{N_0=N, u_0=u_b, v_0=v_b} \quad (2)$$

assuming a pencil beam center (u_b, v_b) according to the regular grid and a constant number of protons N which is equal for all pencil beams.

II.D.3. Optimization of pencil beam weights

Using the F_b as basis functions, it is possible to generate an arbitrary counts field C^α for rotation angle α by finding weights w_b^α , such that C^α is expressed as a linear combination of the reference counts F_b from equation (2). Weights were found by minimizing the squared deviation, and therefore

$$w_b^\alpha(C^\alpha) = \arg \min_{w_b^\alpha} \iint du dv \left(C^\alpha(u, v, 0) - \sum_b w_b^\alpha F_b(u, v, 0) \right)^2. \quad (3)$$

Integration was performed over u and v , but only the isocenter binning depth $d = 0$ was considered. Optimization was performed using the method of Nelder and Mead.⁴¹

II.E. Proposed algorithm for fluence field optimization

Fluence field optimization requires finding a set of fluence modulation factors $m_b^\alpha \in [0, 1]$ for pencil beam b at rotation angle α , such that the resulting pCT reconstruction best achieves a given image variance target $V_{\text{target}}(x, y, z)$. The proposed method for fluence field optimization is performed in the projection domain (denoted by coordinates (u, v, d) and the rotation angle α) instead of the image domain (denoted by coordinates (x, y, z)). The method is sketched in figure 1 and consists of the following three steps, which will be detailed in sections II.E.1. to II.E.3.:

1. For a given phantom, find the resulting variance $V_{\text{unit}}^\alpha(u, v, d)$ in the projection domain for a unit fluence simulation with $m_b^\alpha = 1$ for all pencil beams.
2. For a given image variance target $V_{\text{target}}(x, y, z)$, find a stack of variance levels in the projection domain $V_{\text{target}}^\alpha(u, v, d)$ that yields the image variance target.
3. Calculate the pixel-wise counts target $C_{\text{target}}^\alpha(u, v, d)$. Then, optimize weights that yield the counts target according to equation (3).

The algorithm extends ideas from literature for x-ray CT^{21,22} to requirements of pCT such as the three-dimensional projections due to distance-driven binning³⁹ and a more complex noise model.^{33,34} It is, to our knowledge, not equivalent to any existing approach as it is performed in projection domain and computationally feasible without simplification to a parallel-beam geometry.

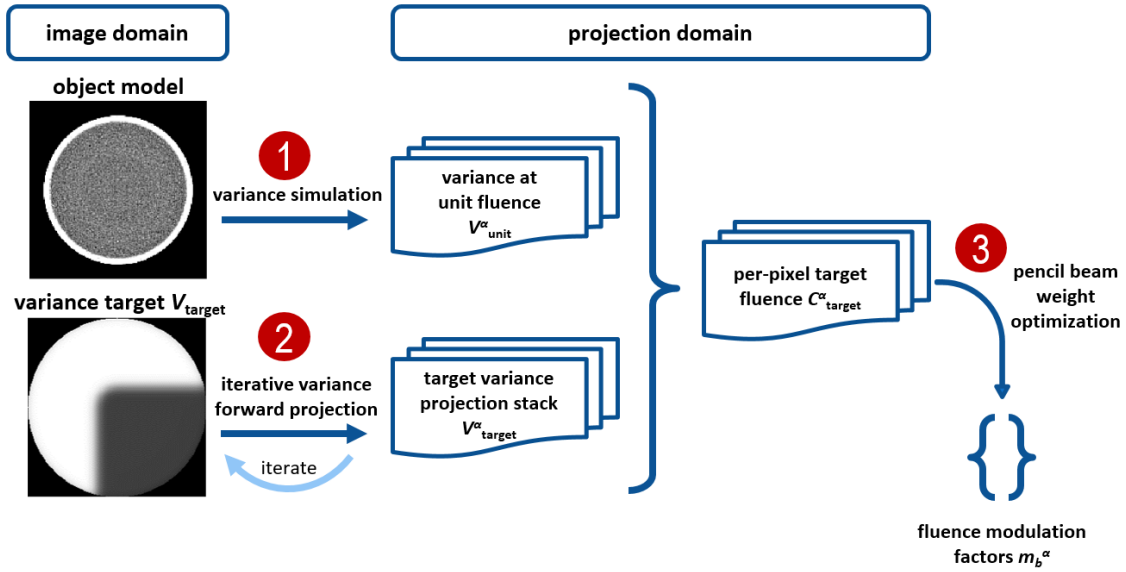


Figure 1: Workflow for optimization of fluence modulation factors m_b^α , given an object model and a variance target V_{target} .

II.E.1. Step 1: Variance at unit fluence prediction

To find variance levels at unit fluence for a given phantom, we employed a Monte Carlo simulation using the beam model described in section II.D. and $m_b^\alpha = 1$ for all pencil beams and rotation angles. This step requires an object model according to section II.C. and resulted in counts $C_{\text{unit}}^\alpha(u, v, d)$, which were reduced compared to the reference counts $F_{\text{unit}}(u, v, d) = \sum_b F_b(u, v, d)$ due to interactions with the object. For every point (u, v, d) in the projection, a set of $n = C_{\text{unit}}^\alpha(u, v, d)$ WEPLs, $\{p\}$, was found such that the voxel around (u, v, d) was crossed by the most likely path of each of the selected protons.³⁹ The unit fluence variance was then the squared error of the mean

$$V_{\text{unit}}^\alpha(u, v, d) = \text{Var}[\{p\}] / C_{\text{unit}}^\alpha(u, v, d). \quad (4)$$

Given a variance projection stack $V_{\text{unit}}^\alpha(u, v, d)$ the corresponding image variance $V_{\text{unit}}(x, y, z)$ can be calculated analytically as reconstruction was performed using filtered backprojection. Please refer to previous publications^{33,34} for details about variance calculations for pCT and for variance reconstruction in general.⁴²

II.E.2. Step 2: Iterative variance forward projection

Finding a stack of variance projections $V_{\text{target}}^\alpha(u, v, d)$ whose variance reconstruction³³ yields a given image variance target $V_{\text{target}}(x, y, z)$ is a problem with a large set of solutions. We therefore aimed to find the inverse operation of variance reconstruction,⁴² i.e. a “variance forward projection.” An initial guess $V_0^\alpha(u, v, d)$ could be obtained by performing ray-tracing⁴³ through the image variance target $V_{\text{target}}(x, y, z)$ followed by a ramp-filtration. The additional filtration was motivated by the fact that variance reconstruction is very close to a simple unfiltered backprojection.⁴² Since ray-tracing is the inverse operation to filtered backprojection, an additional ramp-filtration was required. While such forward- and backprojection yield V_{target} again, this often yields unphysical negative variance projection values and amplifies noise. Therefore, a median filter was applied to the ramp-filtered projections followed by thresholding to positive values.

To minimize the error introduced by thresholding, we employed an iterative approach by applying variance reconstruction to the i -th set of variance projections $V_i^\alpha(u, v, d)$ yielding a variance volume $V_i(x, y, z)$. Again, using ray-tracing, the difference volume $V_{\text{target}}(x, y, z) - V_i(x, y, z)$ was forward-projected and added to the current stack of variance projections. In every iteration, variance projection values were forced to be positive. This will converge to a set of physical (i.e. strictly positive) variance projections that yield an image variance approaching $V_{\text{target}}(x, y, z)$.

II.E.3. Step 3: Fluence optimization

By definition, the variance projection values in equation (4) are inversely proportional to the number of contributing protons C . Therefore, the pixel-wise counts required to achieve the variance target could be calculated as $(V_{\text{unit}}^\alpha/V_{\text{target}}^\alpha) \cdot C_{\text{unit}}^\alpha$. However, for low counts, we need to consider that C follows a Poisson distribution (contrary to a normal distribution at sufficiently high counts) and therefore an additional correction function

$$k(C) = C \cdot \sum_{n'=1}^{\infty} P_C(n') \cdot \beta_{n',C} = C^2 \sum_{n'=1}^{\infty} \frac{P_C(n')}{n'} \quad (5)$$

needs to be introduced, where $P_C(n') = C^{n'} \exp(-C)/n'!$ is the Poisson probability of detecting n' protons instead of the expectation value of C and $\beta_{n',C} = C/n'$ is the relative

change in variance if n' instead of C protons were detected. The function $k(C)$ was stored in a lookup table for all relevant integer values of C up to 300 by numerically calculating the infinite sum for 1000 summands. Since $\lim_{C \rightarrow \infty} k(C)/C = 1$ and $k(300)/300 = 1.0033$ we assumed $k(C) = C$ for all $C > 300$. Furthermore, $k(C)$ was thresholded to return at least $C_{\min} = 8$ protons to avoid detector elements with missing information.

We used an optimization according to equation (3) to find pencil beam weights $w_b^\alpha(C_{\text{target}}^\alpha)$ which achieve the pixel-wise projection counts target of

$$C_{\text{target}}^\alpha(u, v, d) = k \left[\frac{V_{\text{unit}}^\alpha(u, v, d)}{V_{\text{target}}^\alpha(u, v, d)} \cdot C_{\text{unit}}^\alpha(u, v, d) \right]. \quad (6)$$

Due to the fact that C_{unit}^α and C_{target}^α are both affected by interactions with the object, the optimization also needed to be performed for unit fluence allowing for an elimination of the effect of attenuation and scattering. This resulted in fluence modulation factors

$$m_b^\alpha = \frac{w_b^\alpha(C_{\text{target}}^\alpha)}{w_b^\alpha(C_{\text{unit}}^\alpha)} \quad (7)$$

with numerator and denominator as defined in equation (3). Due to the normalization, these factors were corrected for interactions with the object and thus could be used to simulate an FMpCT scan according to section II.D.1..

II.E.4. Reference approach

A simpler approach for fluence field optimization, which was used in previous works,³¹ is to perform a binary modulation with two fluence levels. In image domain, a ROI is defined as a set of voxels that should be imaged with high fluence. A pencil beam is assigned a high imaging fluence if its central axis intersects the ROI, and a low imaging fluence otherwise. The fluence modulation factors were

$$m_b^\alpha = \begin{cases} 1 & \text{if intersecting} \\ \gamma & \text{otherwise} \end{cases}, \quad (8)$$

where $0 < \gamma < 1$ is the modulation strength, which was chosen to be equal to the contrast of the variance prescription of the proposed method.

II.F. Simulation study

In a simulation study we prescribed three different image variance targets, which can be appreciated in figure 2: (1) constant variance V_{ROI} throughout the imaged object; (2) FMpCT

prescription A (variance V_{ROI} inside one quadrant of the imaged object and $4 \cdot V_{\text{ROI}}$ elsewhere); and (3) FMpCT prescription B (V_{ROI} inside a central rectangular region and $4 \cdot V_{\text{ROI}}$ elsewhere). Variance targets are used in step 2 of the proposed algorithm, and therefore independent of the imaged object. In agreement to previous investigations³¹ the prescription contrast of 4 was chosen such that it is higher than the variance dynamic range of a unit fluence scan,³⁴ but reasonably achievable without expecting regions with vanishing counts or distortions of RSP accuracy.

Previous investigations³⁴ have shown that a uniform fluence does not yield a constant variance for pCT. Therefore, the constant variance prescription is the most dose-efficient image, if the complete image is required for diagnosis. Prescriptions A and B model two treatment scenarios, where the treatment beam path is coming from 0 and 90 degrees in A and from 90 and 180 degrees in B. Prescriptions were slightly blurred as sharp gradients in image variance cannot be achieved due to the ramp filtration involved in reconstruction. Throughout this work we use the nomenclature “constant”, “A” and “B” to refer to the three prescriptions.

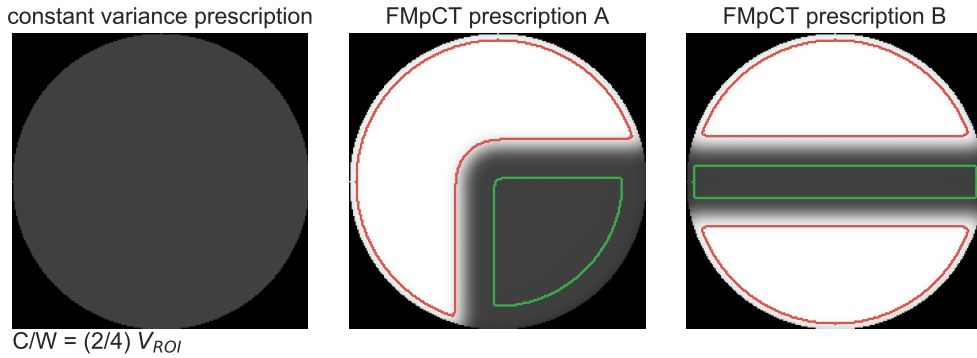


Figure 2: Three different image variance targets for the simulation study. The ROI region and the out-of-ROI region are indicated in green and red respectively. The display center (C) and window (W) is noted below the figure.

For all phantoms we first simulated a high dose unit fluence dataset with $m_i^\alpha = 1$. The mean incident proton fluence was chosen to be 133 mm^{-2} such that it yielded a typical imaging dose for pCT of about 1.4 mGy ,¹² when summed over all projections. We then chose the value of V_{ROI} for each phantom as the 95-th-percentile value of the variance in the unit fluence scan. For the water phantom this was $V_{\text{ROI}} = 4.61 \times 10^{-4}$, for the CTP404 phantom $V_{\text{ROI}} = 5.89 \times 10^{-4}$, and for the head phantom $V_{\text{ROI}} = 11.96 \times 10^{-4}$. These values

are consistent with previous studies.³⁴

For the CTP404 phantom RSP values of the phantom body and of two inserts inside the ROI were evaluated and compared to the unit fluence scenario. The body consisted of epoxy (RSP = 1.144), and inserts were made from Teflon (RSP = 1.791) and polymethylpentene (RSP = 0.883). RSP values were calculated with GEANT4 at a proton energy of 150 MeV and agreed with previous experiments.³⁵

For a fair comparison of imaging doses, we computed the 95-th-percentile variance value v_{95}^{ROI} inside the ROI (inside the whole phantom for unit fluence) and calculated a linear correction factor $\eta = v_{95}^{\text{ROI}}/V_{\text{ROI}}$. Doses and counts were multiplied by η , variances were multiplied by $1/\eta$. The choice of the 95-th-percentile value over the mean or the maximum value is a compromise between the requirement that variances should be at V_{ROI} or lower, and tolerating outliers. As the water and the CTP404 phantom were thin, the percentile value was calculated only within the displayed central slice. For the head phantom, which covered the entire height of the detector aperture, it was calculated over the full volume. To avoid the variance evaluation being dominated by increased noise at the hull of the phantom as discussed in previous works,^{33,34} we determined the shape of the hull by setting an RSP threshold of 0.5 and eroding the hull by 7 mm. Values outside this region were disregarded. The ROI region and the out-of-ROI region are indicated in figure 2 for fluence modulations A and B.

III. Results

III.A. Gaussian pencil beam model

In an experimental dataset without phantom we determined the beam spreads of the Gaussian beam model to be $\sigma_u = (4.04 \pm 0.08) \text{ mm}$ and $\sigma_v = (5.24 \pm 0.09) \text{ mm}$. The divergence was $\delta_u = (5.2 \pm 0.6) 10^{-4} \text{ mm}^{-1}$ and $\delta_v = (5.8 \pm 1.4) 10^{-4} \text{ mm}^{-1}$. The beam spread in the u direction was significantly smaller compared to the beam spread in v direction. Divergence in the u and v direction did not differ outside of the uncertainty bounds. The distances from the isocenter to a virtual source were $1/\delta_u = (1.9 \pm 0.2) \text{ m}$ and $1/\delta_v = (1.7 \pm 0.4) \text{ m}$, which agrees with the position of the scanning magnets, which is 1.8 m from the isocenter. The stated parameters were used in all following evaluations.

III.B. Variance optimization

III.B.1. Iterative variance forward projection

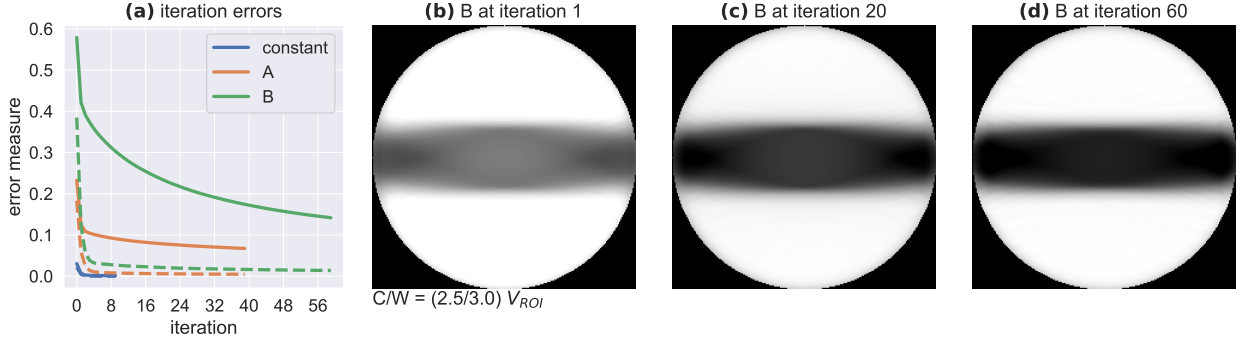


Figure 3: (a) Root-mean-square error (solid) and mean error (dashed) as a function of the iteration number of the three image variance targets. (b) – (d) Reconstructed variance volumes for prescription B for different iterations. The display center (C) and window (W) is noted below the figure.

For step 2 of the proposed method, figure 3 (a) shows error measures as a function of the iteration number. The root-mean-square (RMS) error as well as the mean error between the current variance volume $V_i(x, y, z)$ and the variance target $V_{\text{target}}(x, y, z)$ are calculated within the field-of-view. The fastest convergence is observed for the constant variance prescription, while both FMpCT prescriptions A and B show a remaining RMS error that only reduces slowly in every iteration. The mean error quickly drops to zero within the first iterations. The relative change in RMS error for all prescriptions was below 1 % per iteration when they were stopped. Figure 3 (b) to (d) show $V_i(x, y, z)$ for prescription B at three different iterations. At iteration 20, the high-variance region has reached the correct value, while in the low-variance region artifacts remain, but decrease up to the last iteration.

III.B.2. Fluence optimization

To validate the use of the correction function $k(C)$, figure 4 shows $k(C)/C$ together with the relative increase of the image variance V_C at mean counts C . The relative increase is calculated as $(V_C \cdot C)/(V_{C_\infty} \cdot C_\infty)$ for $C_\infty = 310$ for simulated pCT data. Both curves agree, which shows that variance increases overproportionally for low counts and that the correction function $k(C)$ describes this well.

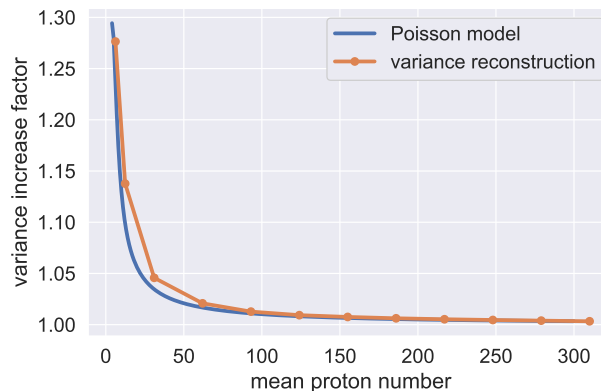


Figure 4: Overproportional increase of image variance with decreasing counts in a simulation with varying mean proton number C and agreement with the fluence correction function $k(C)/C$.

Figure 5 shows intermediate steps of the fluence optimization for the pediatric head phantom and variance prescription A. All projection data are shown as sinograms plotted as a function of the detector position in u direction and the rotation angle. Only data for $v = d = 0$ are shown. In figure 5 (a), variance at unit fluence $V_{\text{unit}}^{\alpha}(u, 0, 0)$ is shown (step 1 of the algorithm), which is high at the periphery of the object and around heterogeneities, as discussed in previous works.³⁴ Figure 5 (b) shows the variance target $V_{\text{target}}^{\alpha}(u, 0, 0)$ as a result of the iterative optimization (step 2). Figure 5 (c) shows the pixel-wise counts target for fluence modulation $C_{\text{target}}^{\alpha}(u, 0, 0)$ (step 3) as given by equation (6). Parts of the variance target in (b) are assigned a value of 0, and receive the unit fluence in (c). In figure 5 (d), the counts target is fitted by the pencil beam model to get the weights required for fluence modulation (also step 3). This can be calculated as $\sum_b w_b^{\alpha} F_b(u, v, d)$. Some small features of (c) are not present in (d) if they are smaller than the extension of a pencil beam.

III.C. Simulation study

Figures 6 and 7 show simulated fluence modulations for all phantoms. RSP, variance and dose maps are shown together with the counts sinograms. For the water phantom imaged with unit fluence (figure 6 (a)), counts and dose were homogeneous throughout the phantom, variance was reduced in the center. This reduction was compensated in figure 6 (b) for the constant variance target, where instead counts and imaging dose were reduced in the center and variance was homogeneous across the phantom, except for a steep increase at the hull.

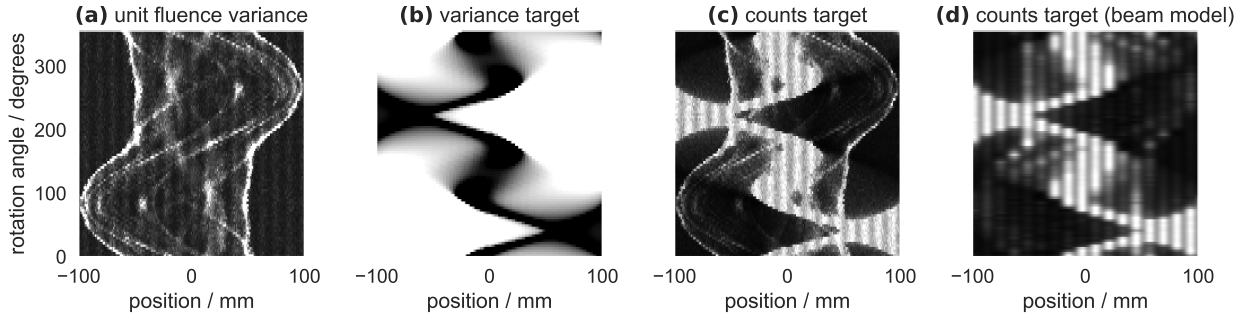


Figure 5: Intermediate results of the fluence optimization process for the pediatric head phantom and the orthogonal beams variance target: (a) unit fluence variance $V_{\text{unit}}^{\alpha}(u, 0, 0)$, (b) variance target $V_{\text{target}}^{\alpha}(u, 0, 0)$, (c) pixel-wise target counts $C_{\text{target}}^{\alpha}(u, 0, 0)$, and (d) target counts as fitted by the beam model. Data are shown as a function of the rotation angle α and the detector coordinate u . For display a center of 0.4 mm^2 and a window of 0.8 mm^2 has been applied for variances, and a center of 80 and a window of 160 for counts.

The fluence modulations in figure 6 (c) and (e) for variance targets A and B can already be appreciated in the RSP maps. Variance levels followed the prescription with a sharp gradient. For prescription A some streaks of high variance were observed within the ROI. Using the reference approach in figure 6 (d) and (f), conformity of variance and dose maps with the ROI was degraded, in particular for prescription B, where variance and dose are at the same level as in the unit fluence scan for most of the phantom and the change in variance cannot be seen in the RSP maps. In the counts sinograms, regions of increased counts roughly agreed with those using the optimization, but were uniform, as required. Instead, using the optimization, a heterogeneous counts pattern was observed.

For the CTP404 phantom (figure 7 (a,b)) and the head phantom (figure 7 (c,d)), variance increased around heterogeneities both in unit fluence and fluence-modulated scans. For the head phantom in particular the palate exhibited locally elevated variance levels. The fluence modulation with prescription A was less conformal, compared to those of the water phantom. In particular for the CTP404 phantom variance contrast was impaired. Counts sinograms for prescription A in figure 6 (c) and figure 7 (b,d) are similar, but phantom-specific differences are noticeable.

Mean imaging doses are summarized in figure 8, where for fluence modulations the mean dose over the whole phantom as well as mean doses in the ROI region and the out-of-ROI region are reported. For the water phantom, prescribing constant variance resulted in a dose reduction of 8.9 % compared to the unit fluence dose. For the region-of-interest fluence

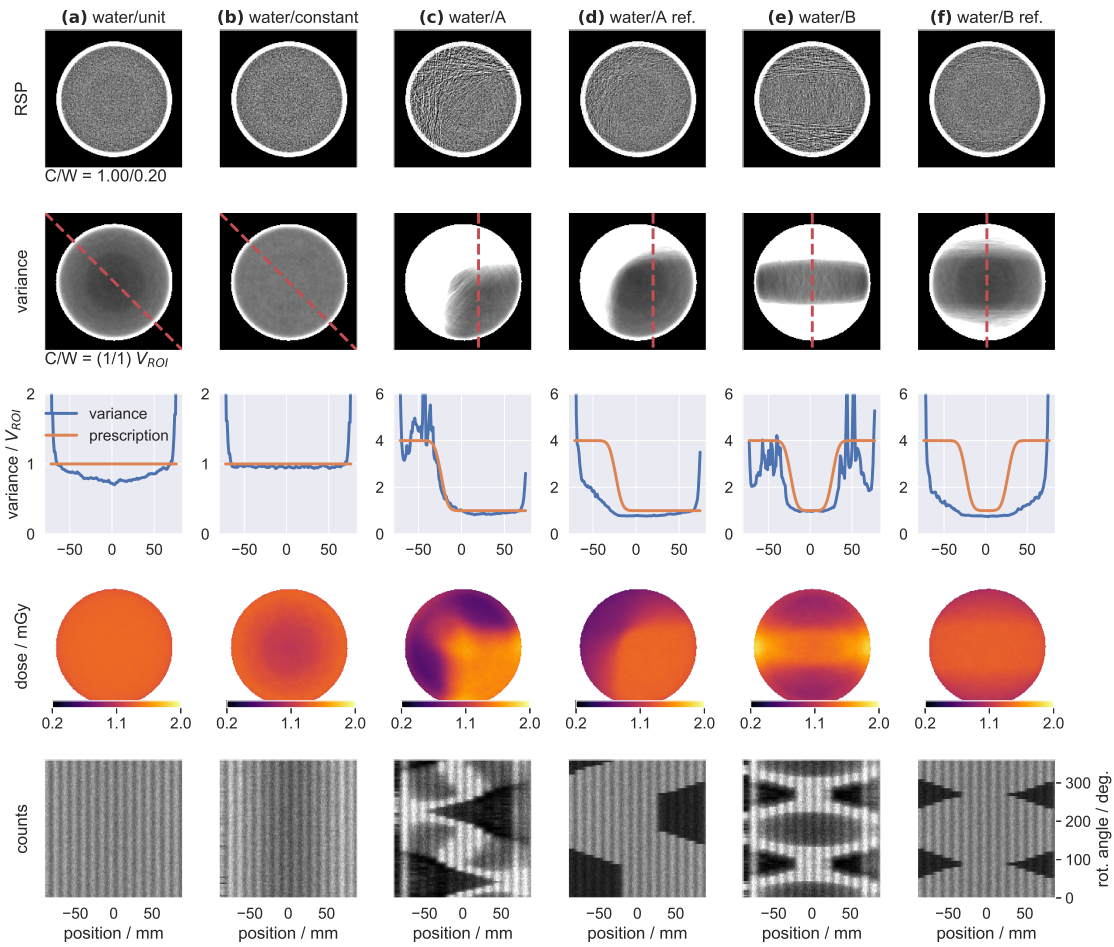


Figure 6: Simulation study for the water phantom and variance targets as indicated in the titles. Sinograms are shown for $v = d = 0$. Center (C) and window (W) settings for display of RSP and variance values are given.

modulations, dose saving outside the ROI was 40.5 % for prescription A and 25.7 % for prescription B. Using the simple reference approach, dose reductions were less pronounced and dropped to 29.2 % and 13.2 % respectively. For the FMpCT prescription A and the CTP404 phantom as well as the head phantom, dose savings outside the ROI were slightly lower compared to the 40.5 % of the water phantom (35.4 % and 38.9 % respectively). For all phantoms, fluence modulations A and B achieved a lower dose outside the ROI compared to the unit fluence, but after normalization with η required a higher dose inside the ROI by 9.2 % to 19.2 %. Doses inside the ROI were approximately constant for the reference approach. Mean doses over the whole phantom were reduced by 7.2 % to 13.1 % using the reference approach and by 9.8 % to 18.6 % for the FMpCT optimizations.

413 For the CTP404 phantom, the two inserts and the body inside the ROI had an RSP
414 value of 1.776, 0.881, and 1.143, compared to 1.776, 0.879, and 1.143 for the unit fluence
415 case.

416 Figure 9 shows the head phantom with unit fluence (a,b) and for the constant variance
417 target (c,d) both in a sagittal view (a,c) and a coronal view (b,d). Dose is homogeneous
418 for the unit fluence imaging, but the variance is notably lower in the back of the head and
419 around the spinal cord compared to regions around the palate and the nasal cavities. These
420 variations were compensated for in the fluence modulations achieving more homogeneous
421 variance levels at reduced doses in regions where variance was low for unit fluence. Mean
422 dose over the whole phantom was 1.15 mGy compared to 1.37 mGy in the unit fluence case
423 (16.0 % reduction). Around the palate and the nasal cavities, dose is increased in the fluence-
424 modulated scan, which is not expected and may be due to the normalization by η .

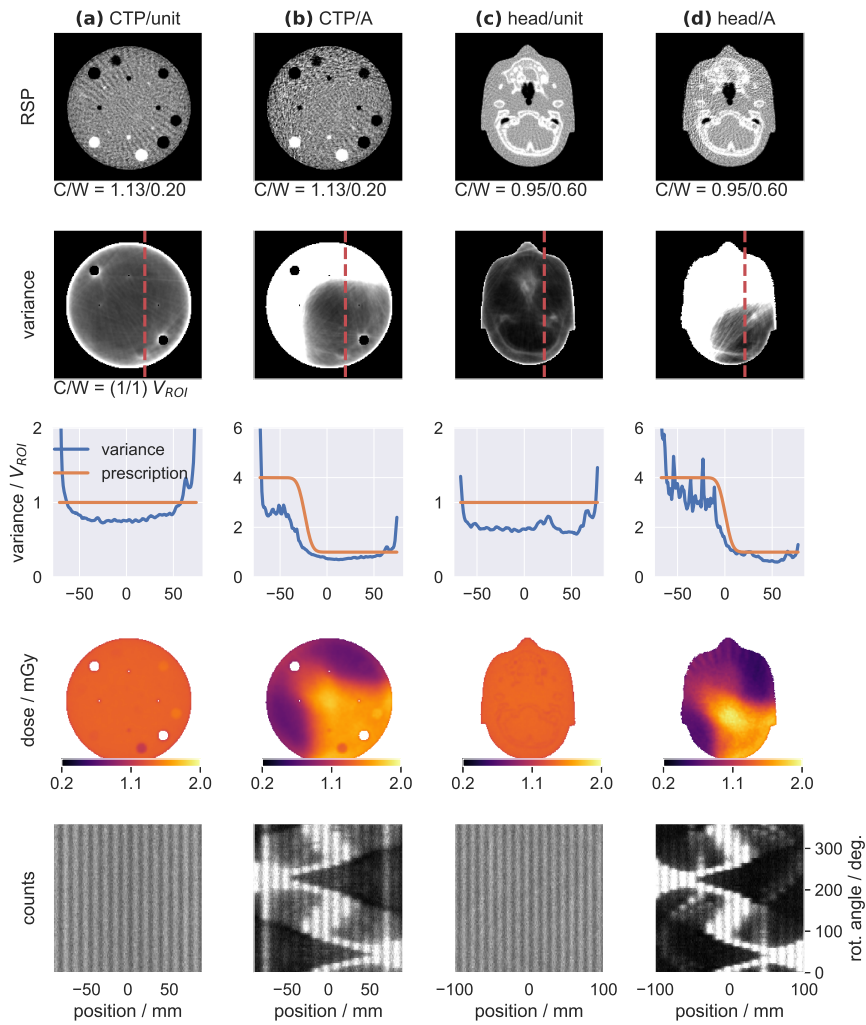


Figure 7: Simulation study for the CTP404 and the head phantom, and variance targets as indicated in the titles. Sinograms are shown for $v = d = 0$. Center (C) and window (W) settings for display of RSP and variance values are given.

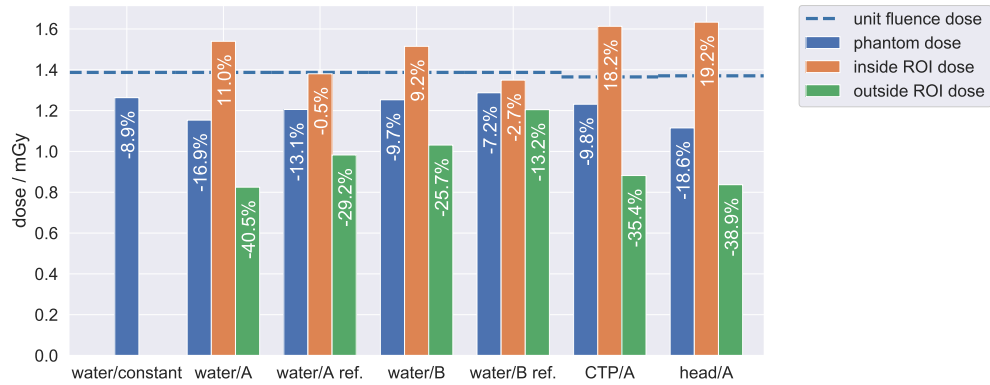


Figure 8: Mean imaging doses for the simulation study. The dashed line indicates the unit fluence dose while bars show the average phantom dose and doses inside and outside the ROI. The relative dose change compared to unit fluence dose is given inside the bars. Unit fluences were equal for all phantoms, but unit fluence doses differed slightly.

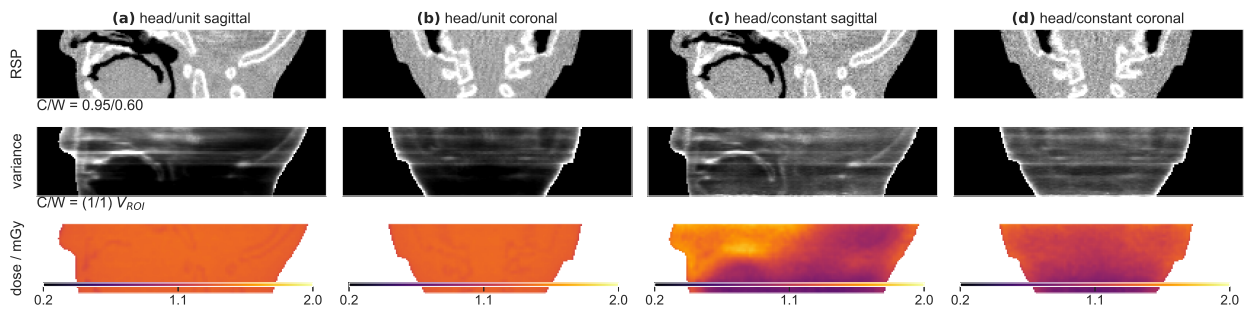


Figure 9: Simulation study for the pediatric head phantom with unit fluence (a), (b) and the constant variance target (c), (d). Row by row, the RSP, variance, and imaging dose are shown. Sagittal and coronal views are shown. Center (C) and window (W) settings for display of RSP and variance values are given.

IV. Discussion

IV.A. Gaussian pencil beam model

We found parameters of a Gaussian pencil beam model that allowed us to describe pencil beams at arbitrary fluences and positions. This is a key component of the fluence modulation scheme, as it allows to find a linear combination of a regular grid of pencil beams that achieves the required counts as calculated by our algorithm. Uncertainty bounds for fits in v direction were consistently larger than those in u direction, in particular for the divergence parameter δ . This was because the detector aperture is smaller in u direction and less datapoints were available. The beam spread σ_v was significantly larger than σ_u . While this anisotropy is not expected for clinical operation, it may have been caused by operating the beam line in research mode and modifying beam optics settings to keep proton fluence low and viable for the scanner. For future experimental studies, certain model parameters, such as the beam energy spread, may require adjustment to exactly match experimental variance levels.

IV.B. Variance optimization

IV.B.1. Iterative variance forward projection

Using an iterative approach, we calculated stacks of variance projections that yield a desired variance map in image space. Depending on the complexity of the variance prescription, this required a different amount of iterations and a non-zero RMS error remained. The easiest case (constant variance target), did not require negative variance values (a constant stack of variance projections would yield a constant image variance) and therefore converged quickly. The two inhomogeneous variance targets A and B did suffer from the positivity requirement and therefore only slowly converged towards a reduced RMS error. While with negative variance values, a (close to) zero RMS error would be possible, this was not the case when requiring physical variance values. The variance target stacks therefore already contained an inherent error, which impacted the achievable variance contrast. However, it did not impact fluence modulation in general, as the prescribed fluences could be rescaled, such that V_{ROI} was achieved inside the ROI.

IV.B.2. Fluence optimization

We calculated the counts target according to equation (6), which could run into a lower and an upper limit. Firstly, to ensure that that data was available throughout the projection, we required at least C_{\min} protons in every pixel. Secondly, to avoid unreasonably high imaging doses, only fluence modulation factors $m_b^\alpha \leq 1$ were allowed, even if the variance target from the previous step (iterative variance forward projection) was zero. This was relevant in particular at the hull of the object, which is also a limited area to be traversed by a therapeutic proton beam. Again, both limits impacted achievable variance contrast, but V_{ROI} could be achieved in the ROI by rescaling with η . Due to the limitation to pencil beams with a finite size, small variance features were averaged out, which may impact homogeneity of the achieved variance, in particular for phantoms with strong heterogeneities.

IV.C. Simulation study

We simulated FMpCT scans for different phantoms and variance targets demonstrating two possible applications for dose reduction using fluence modulation: (1) for achieving constant variance throughout the object and (2) concentrating imaging dose in a high image quality ROI and reducing it elsewhere.

The dose reduction for constant variance with the homogeneous water phantom was 8.9 %, which already is considerable. As shown in previous investigations,³⁴ variance for heterogeneous phantoms is dominated by multiple Coulomb scattering, which depends on the local heterogeneity of the phantom. Therefore, variance maps of the head phantom in coronal and sagittal views were varying greatly. Assuming that good image quality is required in the complete field-of-view, a fluence-modulated scan can reduce the imaging dose by 16.0 % compared to a unit fluence scan, without any loss of diagnostic value. Equivalently, the signal-to-noise ratio could have been improved by 35 % at equal dose.

For all phantoms and two different image variance targets we could demonstrate considerable dose savings of 25.7 % to 40.5 % outside of the ROI. At the same time, the imaging dose inside the ROI increased compared to the unit fluence acquisition. Assuming that the ROI agrees with the treatment beam path and that treatment doses are several orders of magnitude higher than imaging doses, this increase is probably not relevant. At the same

time, proton therapy allows for minimal doses outside the treatment beam path, requiring that this advantage is not compromised by frequent imaging. Mean imaging doses over the whole phantom were reduced for all combinations of phantoms and variance targets. Using a sensitometric phantom we showed that RSP accuracy is not compromised by fluence modulation. RSP errors were comparable for modulated and un-modulated scans, and all below 1 %, which is within the magnitude expected from literature.^{12,19,35}

Imaging doses in fluence-modulated scans showed local increases and doses partially spilled out of the ROI. This may have impaired results in this study and could be caused by the fact that optimization was exclusively performed with a variance objective. Future studies should therefore include a dose objective outside of the ROI while keeping the variance objective inside the ROI, further developing ideas from studies for x-ray CT.²¹ Moreover, the optimal choice of the contrast in the image variance prescription should be studied in the future, but is out of scope for this work.

Using a simple intersection-based approach also showed dose savings compared to unit fluence acquisitions. However, dose savings were considerably less compared to the optimized FMpCT scans and conformity of variance with the prescription was degraded. By construction, a prescription of constant variance is not possible with this approach.

Future work should also address the impact of iterative image reconstruction, which is frequently used for pCT imaging.^{44–48} In contrast to the direct filtered backprojection algorithm used in this study, iterative reconstruction employs a regularization method (typically total variation), which reduces noise and whose optimal weight depends on the object and the fluence level.⁴⁹ While most fluence modulation studies for x-ray CT have been performed using filtered backprojection,^{20,21} a first study²³ investigated a joint optimization of the fluence field and a spatially varying regularization parameter in the iterative reconstruction. For pCT, a comparison of iterative and direct reconstruction⁴⁷ showed comparable image quality. Preliminary work of the authors using an iterative reconstruction algorithm⁴⁶ and fluence modulation suggests feasibility of combining the two methods for pCT.

V. Conclusion

We developed a novel method for fluence-modulated proton computed tomography using pencil beam scanning and demonstrated its feasibility in a simulation study. Dose reductions achieved by prescribing uniform variance were considerable, in particular for an anthropomorphic head phantom. This suggests the need for employing non-uniform fluence patterns in future pCT studies, whenever dose efficiency is a key requirement. Furthermore, the proposed method allows us to prescribe arbitrary image variance targets, which were shown to further reduce imaging dose outside of a given region-of-interest. This can be of particular interest in the context of particle therapy and allow for daily imaging at a reduced imaging dose to healthy tissue outside of the treatment beam path.

Acknowledgments

This work was supported by the German Research Foundation (DFG) project #388731804 “Fluence modulated proton computed tomography: a new approach for low-dose image guidance in particle therapy” and the DFG’s Cluster of Excellence Munich–Centre for Advanced Photonics (MAP), by the Bavaria–California Technology Center (BaCaTeC) and by the Franco–Bavarian university cooperation center (BayFrance).

References

- ¹ D. C. Weber, R. Schneider, G. Goitein *et al.*, Spot Scanning-Based Proton Therapy for Intracranial Meningioma: Long-Term Results From the Paul Scherrer Institute, *Int. J. Radiat. Oncol.* **83**, 865–871 (2012).
- ² V. Verma, S. H. Lin, C. B. Simone, and M. P. Mehta, Clinical outcomes and toxicities of proton radiotherapy for gastrointestinal neoplasms: a systematic review, *J. Gastrointest. Oncol.* **7**, 644–664 (2016).
- ³ K. Nakajima, H. Iwata, H. Ogino *et al.*, Clinical Outcomes of Image-Guided Proton Therapy for Stage I Non-small Cell Lung Cancer, *Int. J. Radiat. Oncol.* **99**, E483–E484 (2017).

-
- ⁴ H. Kim, H. Pyo, J. M. Noh *et al.*, Preliminary result of definitive radiotherapy in patients with non-small cell lung cancer who have underlying idiopathic pulmonary fibrosis: comparison between X-ray and proton therapy, *Radiat. Oncol.* **14**, 19 (2019).
- ⁵ G. Landry and C.-H. Hua, Current state and future applications of radiological image guidance for particle therapy, *Med. Phys.* **45**, e1086–e1095 (2018).
- ⁶ L. Nenoff, M. Matter, J. Hedlund Lindmar, D. C. Weber, A. J. Lomax, and F. Albertini, Daily adaptive proton therapy – the key to innovative planning approaches for paranasal cancer treatments, *Acta Oncol.* (2019).
- ⁷ N. Hudobivnik, F. Schwarz, T. Johnson *et al.*, Comparison of proton therapy treatment planning for head tumors with a pencil beam algorithm on dual and single energy CT images, *Med. Phys.* **43**, 495–504 (2016).
- ⁸ P. Wohlfahrt, C. Möhler, K. Stützer, S. Greulich, and C. Richter, Dual-energy CT based proton range prediction in head and pelvic tumor patients, *Radiother. Oncol.* **125**, 526–533 (2017).
- ⁹ V. T. Taasti, C. Bäumer, C. V. Dahlgren *et al.*, Inter-centre variability of CT-based stopping-power prediction in particle therapy: Survey-based evaluation, *Phys. Imaging Radiat. Oncol.* **6**, 25–30 (2018).
- ¹⁰ P. Alaei and E. Spezi, Imaging dose from cone beam computed tomography in radiation therapy, *Phys. Medica* **31**, 647–658 (2015).
- ¹¹ I. Rinaldi, S. Brons, J. Gordon *et al.*, Experimental characterization of a prototype detector system for carbon ion radiography and tomography, *Phys. Med. Biol.* **58**, 413–427 (2013).
- ¹² R. W. Schulte, V. Bashkirov, M. C. Klock *et al.*, Density resolution of proton computed tomography, *Med. Phys.* **32**, 1035–1046 (2005).
- ¹³ R. P. Johnson, V. Bashkirov, L. DeWitt *et al.*, A Fast Experimental Scanner for Proton CT: Technical Performance and First Experience With Phantom Scans, *IEEE Trans. Nucl. Sci.* **63**, 52–60 (2016).
-

- 562 ¹⁴ M. Esposito, C. Waltham, J. T. Taylor *et al.*, PRAVDA: The first solid-state system for
563 proton computed tomography, *Phys. Medica* **55**, 149–154 (2018).
- 564 ¹⁵ L. Volz, P. Piersimoni, V. A. Bashkirov *et al.*, The impact of secondary fragments on
565 the image quality of helium ion imaging, *Phys. Med. Biol.* **63**, 195016 (2018).
- 566 ¹⁶ S. Meyer, F. Kamp, T. Tessonnier *et al.*, Dosimetric accuracy and radiobiological im-
567 plications of ion computed tomography for proton therapy treatment planning, *Phys.*
568 *Med. Biol.* (2019).
- 569 ¹⁷ M. Yang, X. R. Zhu, P. C. Park *et al.*, Comprehensive analysis of proton range un-
570 certainties related to patient stopping-power-ratio estimation using the stoichiometric
571 calibration, *Phys. Med. Biol.* **57**, 4095–4115 (2012).
- 572 ¹⁸ D. C. Hansen, J. Seco, T. S. Sørensen *et al.*, A simulation study on proton computed
573 tomography (CT) stopping power accuracy using dual energy CT scans as benchmark,
574 *Acta Oncol.* **54**, 1638–1642 (2015).
- 575 ¹⁹ G. Dedes, J. Dickmann, K. Niepel *et al.*, Experimental comparison of proton CT and
576 dual energy x-ray CT for relative stopping power estimation in proton therapy, *Phys.*
577 *Med. Biol.* **64**, 165002 (2019).
- 578 ²⁰ S. A. Graham, J. H. Siewerdsen, and D. A. Jaffray, Intensity-modulated fluence patterns
579 for task-specific imaging in cone-beam CT, *Proc. SPIE* **651003** (2007).
- 580 ²¹ S. Bartolac, S. Graham, J. Siewerdsen, and D. Jaffray, Fluence field optimization for
581 noise and dose objectives in CT, *Med. Phys.* **38**, S2–S17 (2011).
- 582 ²² S. S. Hsieh and N. J. Pelc, Control algorithms for dynamic attenuators, *Med. Phys.* **41**,
583 061907 (2014).
- 584 ²³ G. J. Gang, A. Mao, W. Wang *et al.*, Dynamic fluence field modulation in computed
585 tomography using multiple aperture devices, *Phys. Med. Biol.* **64**, 105024 (2019).
- 586 ²⁴ W. Wang, G. J. Gang, J. H. Siewerdsen, and J. W. Stayman, Volume-of-interest imaging
587 using multiple aperture devices, *Proc. SPIE* **1094823** (2019).
-

-
- 588 25 S. Bartolac and D. Jaffray, Compensator models for fluence field modulated computed
589 tomography, *Med. Phys.* **40**, 121909 (2013).
- 590 26 T. P. Szczykutowicz and C. A. Mistretta, Experimental realization of fluence field mod-
591 ulated CT using digital beam attenuation, *Phys. Med. Biol.* **59**, 1305–1326 (2014).
- 592 27 T. P. Szczykutowicz, J. Hermus, M. Geurts, and J. Smilowitz, Realization of fluence
593 field modulated CT on a clinical TomoTherapy megavoltage CT system, *Phys. Med.*
594 *Biol.* **60**, 7245–7257 (2015).
- 595 28 J. W. Stayman, A. Mathews, W. Zbijewski *et al.*, Fluence-field modulated x-ray CT
596 using multiple aperture devices, *Proc. SPIE* **97830X** (2016).
- 597 29 S. M. Huck, G. S. K. Fung, K. Parodi, and K. Stierstorfer, Technical Note: Sheetbased
598 dynamic beam attenuator – A novel concept for dynamic fluence field modulation in
599 xray CT, *Med. Phys.* **46**, 5528–5537 (2019).
- 600 30 G. Dedes, L. De Angelis, S. Rit *et al.*, Application of fluence field modulation to proton
601 computed tomography for proton therapy imaging, *Phys. Med. Biol.* **62**, 6026–6043
602 (2017).
- 603 31 G. Dedes, R. P. Johnson, M. Pankuch *et al.*, Experimental fluence-modulated proton
604 computed tomography by pencil beam scanning, *Med. Phys.* **45**, 3287–3296 (2018).
- 605 32 M. M. Lell and M. Kachelrieß, Recent and Upcoming Technological Developments in
606 Computed Tomography, *Invest. Radiol.* **55**, 8–19 (2020).
- 607 33 M. Rädler, G. Landry, S. Rit, R. W. Schulte, K. Parodi, and G. Dedes, Two-dimensional
608 noise reconstruction in proton computed tomography using distance-driven filtered back-
609 projection of simulated projections, *Phys. Med. Biol.* **63**, 215009 (2018).
- 610 34 J. Dickmann, P. Wesp, M. Rädler *et al.*, Prediction of image noise contributions in
611 proton computed tomography and comparison to measurements, *Phys. Med. Biol.* **64**,
612 145016 (2019).
- 613 35 V. Giacometti, V. A. Bashkirov, P. Piersimoni *et al.*, Software platform for simulation
614 of a prototype proton CT scanner, *Med. Phys.* **44**, 1002–1016 (2017).
-

- 615 ³⁶ S. Agostinelli, J. Allison, K. Amako *et al.*, Geant4 - a simulation toolkit, Nucl. Instru-
616 ments Methods Phys. Res. Sect. A Accel. Spectrometers, Detect. Assoc. Equip. **506**,
617 250–303 (2003).
- 618 ³⁷ V. A. Bashkurov, R. W. Schulte, R. F. Hurley *et al.*, Novel scintillation detector design
619 and performance for proton radiography and computed tomography, Med. Phys. **43**,
620 664–674 (2016).
- 621 ³⁸ R. W. Schulte, S. N. Penfold, J. T. Tafas, and K. E. Schubert, A maximum likelihood
622 proton path formalism for application in proton computed tomography, Med. Phys. **35**,
623 4849–4856 (2008).
- 624 ³⁹ S. Rit, G. Dedes, N. Freud, D. Sarrut, and J. M. Létang, Filtered backprojection proton
625 CT reconstruction along most likely paths, Med. Phys. **40**, 031103 (2013).
- 626 ⁴⁰ V. Giacometti, S. Guatelli, M. Bazalova-Carter, A. Rosenfeld, and R. Schulte, Devel-
627 opment of a high resolution voxelised head phantom for medical physics applications,
628 Phys. Medica **33**, 182–188 (2017).
- 629 ⁴¹ J. A. Nelder and R. Mead, A Simplex Method for Function Minimization, Comput. J.
630 **7**, 308–313 (1965).
- 631 ⁴² A. Wunderlich and F. Noo, Image covariance and lesion detectability in direct fan-beam
632 x-ray computed tomography, Phys. Med. Biol. **53**, 2471–2493 (2008).
- 633 ⁴³ P. M. Joseph, An Improved Algorithm for Reprojecting Rays through Pixel Images,
634 IEEE Trans. Med. Imaging **1**, 192–196 (1982).
- 635 ⁴⁴ S. N. Penfold, A. B. Rosenfeld, R. W. Schulte, and K. E. Schubert, A more accurate
636 reconstruction system matrix for quantitative proton computed tomography, Med. Phys.
637 **36**, 4511–4518 (2009).
- 638 ⁴⁵ S. N. Penfold, R. W. Schulte, Y. Censor, and A. B. Rosenfeld, Total variation superior-
639 ization schemes in proton computed tomography image reconstruction, Med. Phys. **37**,
640 5887–5895 (2010).
- 641 ⁴⁶ D. Hansen, N. Bassler, T. Sørensen, and J. Seco, The Image Quality of Ion Computed
642 Tomography at Clinical Imaging Dose Levels, Med. Phys. **41**, 111908 (2014).
-

- 643 ⁴⁷ D. Hansen, T. Sørensen, and S. Rit, Fast reconstruction of low dose proton CT by
644 sinogram interpolation, *Phys. Med. Biol.* **61**, 5868–5882 (2016).
- 645 ⁴⁸ B. Schultze, Y. Censor, P. Karbasi, K. E. Schubert, and R. W. Schulte, An Improved
646 Method of Total Variation Superiorization Applied to Reconstruction in Proton Com-
647 puted Tomography, *IEEE Trans. Med. Imaging*, epub ahead of print (2019).
- 648 ⁴⁹ Z. Tian, X. Jia, K. Yuan, T. Pan, and S. B. Jiang Low-dose CT reconstruction via
649 edge-preserving total variation regularization, *Phys. Med. Biol.* **56**, 5949–5967 (2011).
-